Fabricating Surface-Functionalized CsPbBr$_3$/Cs$_4$PbBr$_6$ Nanosheets for Visible-Light Photocatalytic Oxidation of Styrene

Ping Qiu[1], Qiuhe Wang[1,2], Yizhou Zhao[2], Yi Dai[2], Yuanyuan Dong[2], Changli Chen[2], Qi Chen[2] and Yujing Li[2]*

[1] School of New Energy and Materials Science, China University of Petroleum, Beijing, China, [2] Beijing Key Laboratory of Construction Tailorable Advanced Functional Materials and Green Applications, School of Materials Science and Engineering, Beijing Institute of Technology, Beijing, China

The halide perovskite (PVSK) material, an excellent light absorber with fast carrier kinetics, has received increased attention as a potential photocatalyst for organic synthesis. Herein, we report a straightforward synthesis of chemically modified halide perovskite and its application as an efficient photocatalyst to convert styrene into benzaldehyde. A simple method is employed to synthesize the chemically modified CsPbBr$_3$/Cs$_4$PbBr$_6$ nanosheets by using ZrCl$_4$ to simultaneously achieve the Cl doping and the surface modification with Zr species. The photocatalytic oxidation rate of styrene to benzaldehyde catalyzed by surface-modified CsPbBr$_3$/Cs$_4$PbBr$_6$ nanosheets under visible light can reach 1,098 μmol g^{-1} h^{-1}, 2.9 times higher than that of pristine CsPbBr$_3$/Cs$_4$PbBr$_6$ nanosheets (372 μmol g^{-1} h^{-1}). The enhanced photocatalytic performance may originate from the modified band structure induced by the synergistic effect of Cl doping and surface modification, whereby the same methodology can be applied to MAPbBr$_3$. This work demonstrates the surface modification of PVSK materials and their potential as efficient photocatalyst toward organic synthesis.

Keywords: halide perovskite, photocatalytic oxidation, surface functionalization, benzaldehyde, doping

INTRODUCTION

In recent years, halide perovskite (PVSK) material has received enormous attention due to its unique optoelectronic properties as light-absorbing material in solar cell devices. Based on their excellent photosensitivity, wide range of visible-light absorption (Yang et al., 2017), long carrier lifetime (Yang et al., 2015, 2016), and diffusion length (Xing et al., 2013; Dong et al., 2015), the halide perovskite material possesses the basic physicochemical properties of a good photocatalyst. Besides, the low cost, feasible processability, and adjustable energy levels of band edge make the PVSK a promising candidate for photocatalyst (Chen et al., 2015). However, the PVSK, when used alone, suffers from poor stability and difficulty in functionalization for photocatalysis. SnS$_2$, Au, graphene oxide, and TiO$_2$ have been employed to composite with PVSK as photocatalyst for organic synthesis and other reactions (Huang et al., 2018; Feng et al., 2019; Wang Q. et al., 2019; Wang X. et al., 2019), but very little effort has been made to address the surface of PVSK for efficient photocatalytic process.

Benzaldehyde plays a vital role in the industrial synthesis of numerous chemicals (Hu et al., 2016; Tong et al., 2016; Oliveira et al., 2017). The commonly used methods to synthesize benzaldehyde include the oxidation of benzyl alcohol, direct oxidation of toluene, hydrogenation of benzoic acid, indirect electrooxidation of toluene, and hydrolysis of benzyl chloride (Yadav and Haldavanekar, 1997; Lv et al., 2010; Nasrollahzadeh et al., 2016), which have problems such as complexity of processing, environmental footprint, high manufacturing cost, etc. Recently, the direct oxidation of styrene to benzaldehyde by environmentally friendly oxidants has attracted attention (Singh and Sinha, 2014; Fu et al., 2016; Narayanan et al., 2016). A number of heterogeneous catalysts have been used for the oxidation of styrene, including noble metal catalysts such as Au (Majeed et al., 2016; Wang et al., 2018), Ag (Gupta et al., 2017), Pt (Luo et al., 2015b), and Pd (Luo et al., 2015a), which have shown excellence in both activity and selectivity. However, high prices and finite reserves limit their practical application. Photocatalytic technique could be an optimistic approach to convert styrene based on non-precious metal with abundant reserves and low cost.

In this study, by employing the functionalized PVSK as the photocatalyst, we achieve the efficient conversion of styrene into benzaldehyde with visible light. We report a one-pot method based on the ligand-assisted precipitation (LARP) (Zhang et al., 2015; Zhu et al., 2019) to synthesize surface-modified $CsPbBr_3/Cs_4PbBr_6$ nanosheets as a visible-light photocatalyst for the oxidation of styrene to benzaldehyde at room temperature using oxygen as the oxidant. We use $ZrCl_4$ in modifying $CsPbBr_3/Cs_4PbBr_6$ nanosheets to enhance the oxidation ability and promote the transfer of carriers. The chemical modification with $ZrCl_4$ and the effect of surface functionalization on the properties of $CsPbBr_3/Cs_4PbBr_6$ are investigated. In addition, the mechanism of the enhanced photocatalytic performance from $ZrCl_4$-$CsPbBr_3/Cs_4PbBr_6$ nanosheets toward the oxidation of styrene is reasonably proposed.

EXPERIMENTAL

Materials

Oleic acid (OAc, 90%, Sigma-Aldrich), n-octylamine (99.0%, Aladdin), N,N-dimethyl-formamide (DMF, 99.9%, Aladdin), cyclohexane (99.0%, Aladdin), methyl acetate (99.9%, Aladdin), n-Hexane (99.0%, Aladdin), styrene (99.9%, Aladdin), cesium bromide (CsBr, 99.9%, Sigma-Aldrich), cesium chloride (CsCl, 99.9%, Sigma-Aldrich), lead(II) bromide (PbBr$_2$, 99.9%, Sigma-Aldrich), and zirconium (IV) chloride (ZrCl$_4$, 99.9%, Sigma-Aldrich). All chemical reagents are used as received.

Preparation: Synthesis of Surface-Modified Perovskite $CsPbBr_3/Cs_4PbBr_6$ Nanosheets

The synthesis employs the ligand-assisted precipitation (LARP) method as illustrated in **Figure 1**. Three precursor solutions were prepared by dissolving 2.0 mmol CsBr in 1.0 ml of H$_2$O, 2.0 mmol PbBr$_2$ in 2.5 ml of DMF, and 0.25 mmol ZrCl$_4$ in 0.2 ml of DMF, respectively. Then, 4 ml of oleic acid and 2 ml of n-octylamine were added to a vigorously stirred cyclohexane (200 ml). The PbBr$_2$ solution, ZrCl$_4$ solution, and CsBr solution were added. A microemulsion started to form and the solution turned from transparent into light yellow. Afterwards, methyl acetate (100 ml) was added to break up the emulsion. The as-synthesized $CsPbBr_3/Cs_4PbBr_6$ nanosheets (named as CPB-Zr-0.25) were separated by centrifugation at 10,000 rpm for 10 min, and washed twice with toluene, dried at 80°C, and collected for storage. By changing the amount of ZrCl$_4$ solution added, CPB-Zr-x ($x = 0.25$, 0.5, 0.75, 1) were obtained. The organic–inorganic hybrid lead halide perovskite materials MAPbBr$_3$ and MAPbBr$_3$-Zr-x nanosheets, named MAPB-Zr-x (MA = $CH_3NH_3^+$, $x = 0.25$, 0.5, 0.75, 1), were obtained with the same protocol by replacing CsBr with MABr. The unmodified $CsPbBr_3/Cs_4PbBr_6$ nanosheets were synthesized with the same procedure except that the ZrCl$_4$ precursor was not added. ZrO$_x$Cl$_y$ was prepared with the above procedure except that
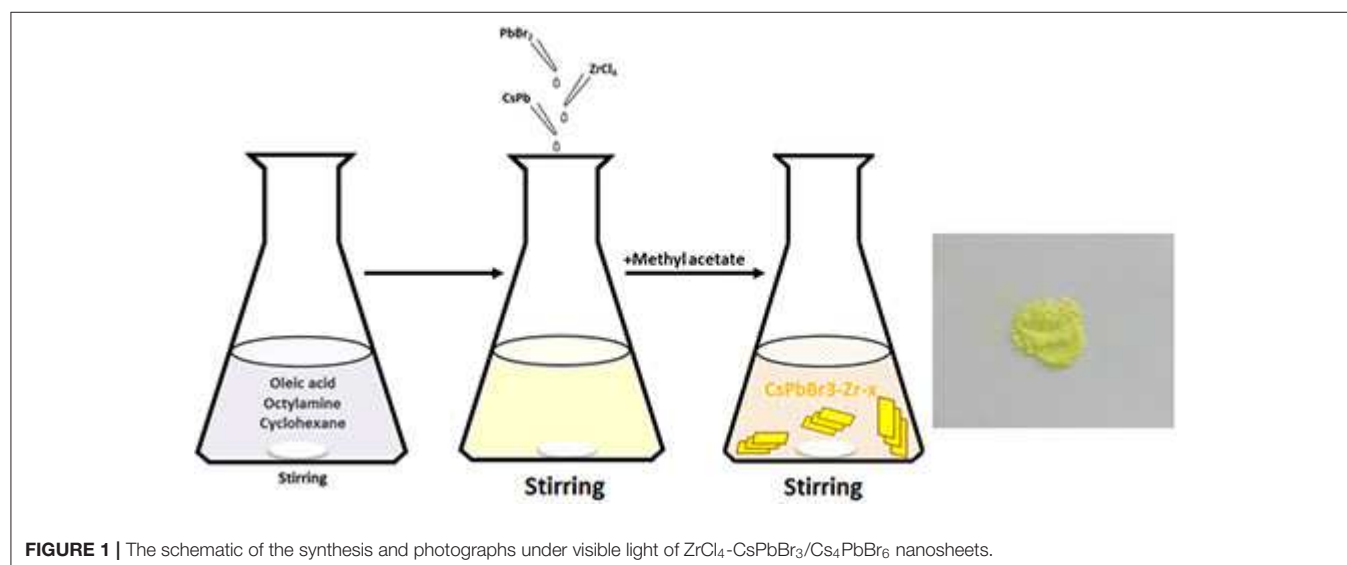

FIGURE 1 | The schematic of the synthesis and photographs under visible light of ZrCl$_4$-CsPbBr$_3$/Cs$_4$PbBr$_6$ nanosheets.

CsBr and PbBr$_2$ were not added, as the comparison for photocatalytic evaluation.

Photocatalytic Activity Measurements

Photocatalytic reactions were conducted in a 20-ml quartz flask matching the Pcx-50c multichannel photochemical reaction device with magnetic stirring at a rate of 500 rpm. The specific procedure was as follows: 20 mg of photocatalyst was dispersed into 9 ml of n-Hexane saturated with molecular oxygen and mixed with 1 ml of styrene. The photocatalytic reaction system was irradiated with a white light-emitting diode (LED) illumination (100 mW cm^{-2}). After reaction for 5 h, the suspension was centrifuged at 10,000 rpm for 8 min and the supernatant was analyzed on Shimadzu GC-2014.

Characterization

X-ray diffraction (XRD) analysis was performed on a Rigaku D/MAX2500 VB2+/PCX-ray diffractometer using Ni-filtered Cu Kα radiation (λ = 1.5406 Å) with a scanning angle (2θ) ranging 10°-60° and the scanning speed at 5°/min. UV-vis diffuse reflectance spectra (DRS) of the samples were studied by a UV-vis spectrophotometer (Perkin Elmer Lambda 950) from 300 to 800 nm. FEI Tecnai G2 F20 was used for high-angle annular dark-field scanning transmission electron microscopy (HAADF-STEM) imaging, and electron energy spectrum (EDX) is obtained from Super-EDX equipped on the TEM FEI G2 (60-300) TEM. The photoluminescence (PL) spectra were acquired by an FLS980 fluorescence spectrometer (steady state, lifetime, phosphorescence, Edinburgh Instruments Ltd.). The steady-state PL was irradiated with 370-nm excitation light. The time-resolved photoluminescence (TRPL) spectra were performed using a 375-nm laser emitter to determine the lifetime of photogenerated carriers. X-ray photoelectron spectroscopy (XPS) was used to study the chemical compositions and the chemical states by a Thermo escalab 250Xi photoelectron spectrometer. Ultraviolet photoelectron spectra (UPS) analysis was performed on British VG Scienta R4000, using He I line as ultraviolet light source with photon energy 21.2 eV, spectrum acquisition range (kinetic energy) 0–22 eV, and step length 0.02 eV. Surface photovoltage (SPV) spectra were conducted in a vacuum chamber with a quartz window. As-prepared samples were placed into a vacuum chamber and illuminated by monochromatic light from a 150-W Xe lamp filtered through an Oriel Cornerstone 130 monochromator (1–10 mW cm^{-2}) within a range of 300–600 nm.

RESULTS AND DISCUSSIONS

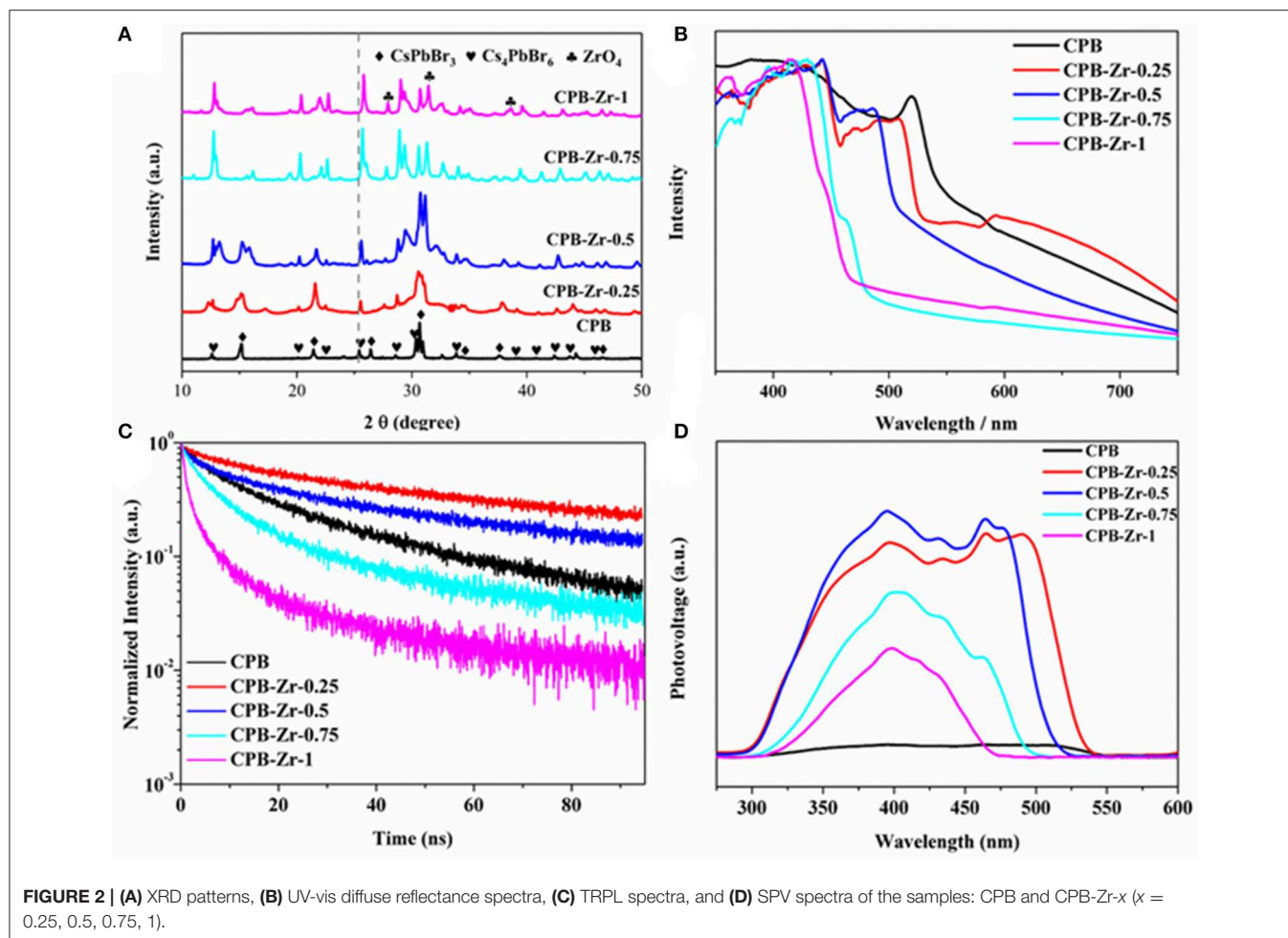### XRD, DRS, TRPL and SPV Spectra Analysis

Figure 2A shows the XRD pattern of CPB and CPB-Zr-x (x = 0.25, 0.5, 0.75, 1). The naked CPB shows a series of peak at 25.3°, 27.1°, 37.8°, and 48.0° (2θ), corresponding to the (001), (110), (002), and (220) crystallographic plane of CsPbBr$_3$ (JCPDS card No. 18-0364), respectively, whereas the peak at 12.55°, 20.25°, 22.56°, and 25.55° (2θ) corresponds to the (012), (113), (300), and (024) crystallographic plane of Cs$_4$PbBr$_6$ (JCPDS card No. 73-2478), indicating that the CPB prepared by LARP

method has a mixed structure of CsPbBr$_3$ and Cs$_4$PbBr$_6$. With the increased amount of ZrCl$_4$, the peak at peaks of CPB-Zr shifts to the higher values with decreased intensity of the diffraction peak. The positive shift of diffraction peaks may largely originate from the inclusion of Cl$^-$ (from ZrCl$_4$) into the lattice, whereby the Cl$^-$ has a smaller radius than that of Br$^-$. When the amount of ZrCl$_4$ further increases, e.g., CPB-Zr-0.75 and CPB-Zr-1, new diffraction peaks start to appear. A thorough search of PDF database turns out that the newly appearing peaks are consistent with the characteristic diffraction peaks of zirconium oxide (JCPDS card No. 1-750). **Figures S1a,b** compare the core-level Cl 2p and Zr 3d XPS spectra from CPB and CPB-Zr-0.75. It can be clearly found the CPB-Zr-0.75 sample shows obvious Cl 2p and Zr 3d peaks, whereas the CPB shows no signal for either spectrum, confirming that the CPB-Zr-0.75 contains Zr and Cl. It can be referred that during the synthesis, part of Cl$^-$ from ZrCl$_4$ dopes into the CPB to replace Br$^-$, while the rest forms ZrO$_2$ on the surface of CsPbBr$_3$/Cs$_4$PbBr$_6$ nanosheets (Xu et al., 2016).

The UV-vis diffuse reflectance spectra of as-prepared CPB and CPB-Zr-x (x = 0.25, 0.5, 0.75, 1) samples are shown in **Figure 2B**. The spectrum of CPB sample displays the absorption in the visible-light region exhibiting an absorption edge at 545 nm, while the CPB-Zr-x samples show blue shift of absorption edge. The ZrCl$_4$ sample cannot absorb light as shown in **Figure S2a**. It is obvious that the chemical functionalization with ZrCl$_4$ can significantly affect the optical absorption feature of CPB. By increasing the amount of ZrCl$_4$, the absorption edge of the samples shows a further blue shift. In particular, the absorption edge of CPB-Zr-1 is at 473 nm. The optical bandgap value can be calculated via the Kubelka–Munk plot shown in **Figure S2b**. The bandgaps are 2.27, 2.36, 2.46, 2.56, and 2.67 eV for CPB, CPB-Zr-0.25, CPB-Zr-0.5, CPB-Zr-0.75, and CPB-Zr-1, respectively. **Figure 2C** displays the PL spectra of all samples. The CPB sample shows a PL peak centered at 521 nm, consistent with the reported values (Shamsi et al., 2016). The trend of PL result is in good agreement with that of the UV-vis diffuse reflectance spectra (**Figure S3**).

The TRPL spectra in **Figure 2C** show the lifetime of photogenerated carriers and the carrier separation kinetics. The fitting results for TRPL spectra of different samples are listed in **Table S1**. It is found that the carrier lifetime increases and then decreases with the increased adding amount of ZrCl$_4$. Compared with the carrier lifetime (24.46 ns) of pure CPB, the CPB-Zr-0.25 shows a longer carrier lifetime at 49.38 ns, but declined gradually to 6.81 ns of CPB-Zr-1. With the small amount of ZrCl$_4$ added in precursor, the Cl$^-$ doped into CPB may result in the elongated carrier lifetime (Jin and Oleg, 2015). With the further increase of added ZrCl$_4$, ZrO$_2$ starts to form on the surface of the CPB and promotes the transfer of carriers and shortens the carrier lifetime.

The SPV spectra shown in **Figure 2D**, employed to evaluate the photochemical charge transfer in the catalyst, reveal that the CPB has very low photovoltage, while the photovoltage increases first with the addition of ZrCl$_4$ and decreases thereafter. It is probably due to the fact that when a small amount of ZrCl$_4$ is added, the surface of CPB is modified and passivated by Zr species to reduce surface defects and increase the photovoltage, while the enlarged bandgap induced by the Cl doping leads to

FIGURE 2 | **(A)** XRD patterns, **(B)** UV-vis diffuse reflectance spectra, **(C)** TRPL spectra, and **(D)** SPV spectra of the samples: CPB and CPB-Zr-x (x = 0.25, 0.5, 0.75, 1).

the blue shift of the absorption edge, consistent with the UV-vis results (Zhao et al., 2016). With further increase of ZrCl$_4$, the bandgap of CPB further expands and drastically reduces the absorption and leads to the decrease of surface photovoltage.

Morphology and Microstructures Analysis

Figure 3 shows the TEM images of CPB and CPB-Zr-x. It can be seen that all samples consist of rectangular nanosheets with a size range of 100–400 nm. As exhibited in **Figures 3d,e**, small particles appear on the surface of CsPbBr$_3$/Cs$_4$PbBr$_6$ nanosheets with the increase of ZrCl$_4$ molar proportion. The high-resolution TEM in **Figure 3f** shows a lattice spacing of 0.589 nm determined by fast Fourier transform (FFT), which corresponds to the spacing between the (100) plane. The lattice spacing of 0.566 nm for CPB-Zr-0.75 corresponds to the distances between the (100) plane. The size of CPB-Zr-x nanosheet decreases with the increased amount of ZrCl$_4$.

To further study the microstructures of CPB modified by ZrCl$_4$, EDX-mapping is used to map out a single nanosheet of CPB-Zr-0.75 sample under HAADF-STEM. As shown in **Figure 4**, the distributions of Cs, Pb, Br, Zr, Cl, and O elements can be visualized. The above elements can almost overlap in the selected region. It implies that Cl$^-$ from ZrCl$_4$ has been

doped into CPB. As for the Zr, its distribution overlaps with the nanosheet implying that some Zr^{4+} may have been doped into the lattice while at the same time it could form ZrO$_2$ nanoparticles that attach to the surface of CPB. It remains difficult to determine the exact amount of the Zr^{4+} that has been doped into the lattice. Considering that the ZrO$_2$ diffraction peaks found in XRD pattern for CPB-Zr-0.75 and CPB-Zr-1, the Zr^{4+} may exist in both forms.

Photocatalytic Performance Evaluation

To evaluate the catalytic performance of the catalyst, the photocatalytic oxidation reaction of styrene was carried out to quantify their photocatalytic activity. The calculated reaction rate is summarized in **Figure 5**. The production rate for CPB is 372 μmol g^{-1} h^{-1}. With the increase of added ZrCl$_4$, it increases first and then declines, whereby the CPB-Zr-0.75 shows the maximum production rate of 1,098 μmol g^{-1} h^{-1}. The comparison sample, ZrO$_x$Cl$_y$, prepared with the same protocol by adding ZrCl$_4$ only, shows the production rate of 52 μmol g^{-1} h^{-1}, suggesting that the nanosheet is critical in increasing the light absorption. One may consider that the improved photocatalytic activity originates solely from the Cl doping. To verify the role of Cl doping, we prepare the samples with the same doping level by
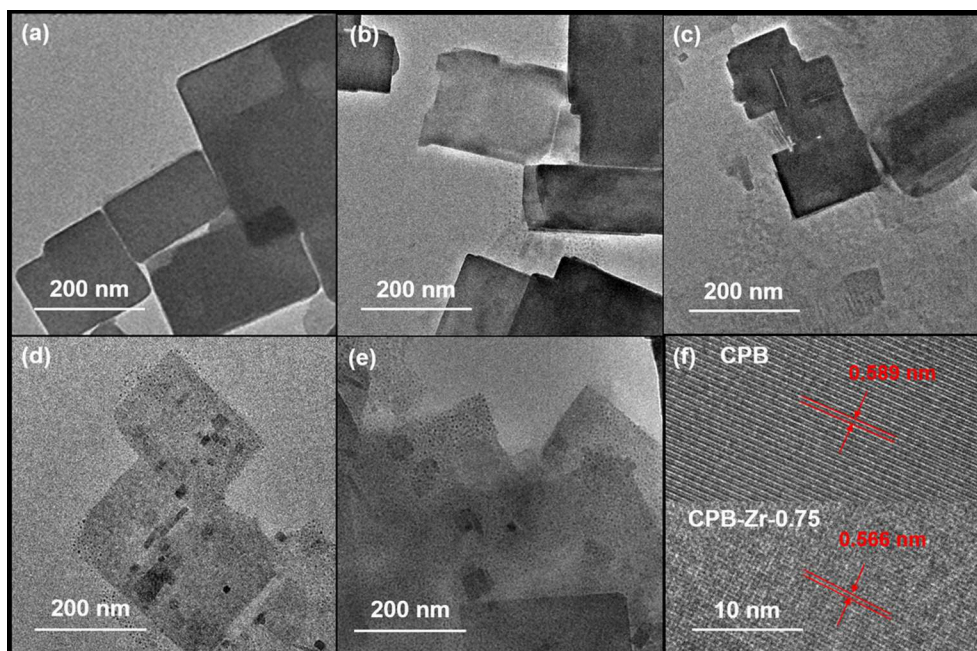
FIGURE 3 | (a–f) TEM image of CPB and CPB-Zr-*x*: **(a)** CPB; **(b)** CPB-Zr-0.25; **(c)** CPB-Zr-0.5; **(d)** CPB-Zr-0.75; **(e)** CPB-Zr-1; **(f)** HRTEM images of CPB and CPB-Zr-0.75.
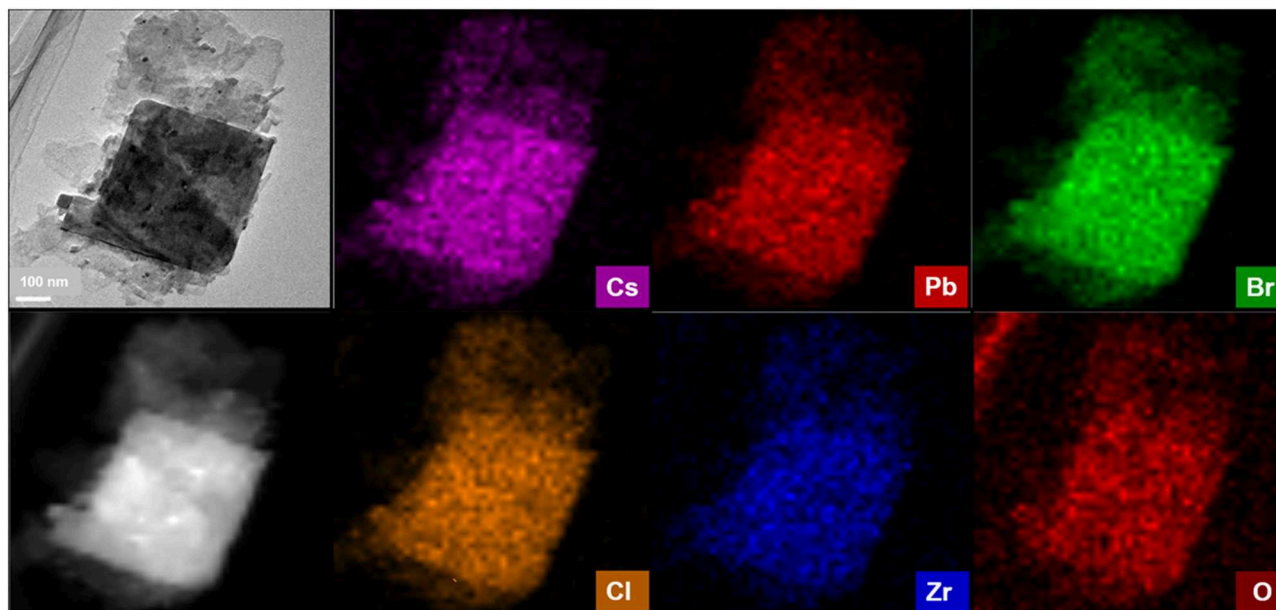

FIGURE 4 | HAADF-STEM image of CPB-Zr-0.75 and the corresponding EDS elemental mapping of Cs, Pb, Br, Cl, Zr, and O in the same area.

substituting the $ZrCl_4$ with CsCl for the synthesis. The CPB-Cl-*x* shows only slight improvement, with the highest production rate 1.09 times that of the pure CPB, as shown in **Figure S4**. It implies that both the surface functionalization of CPB with Zr species and the Cl doping are necessary in largely improving the catalytic performance toward styrene oxidation, possibly through

a synergistic effect between the two methods. It also suggests that the addition of $ZrCl_4$ during the synthesis for the surface modification can "kill two birds with one stone."

It is also known that the halide perovskite is prone to be oxidized. To evaluate the structure and phase after the reaction, the catalysts are collected for structural and

physicochemical analysis with XRD and PL measurements (**Figure S5**), showing that the XRD pattern for the catalyst after
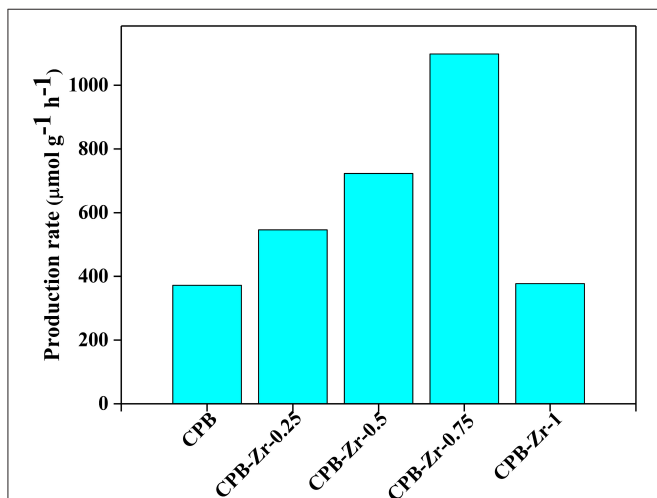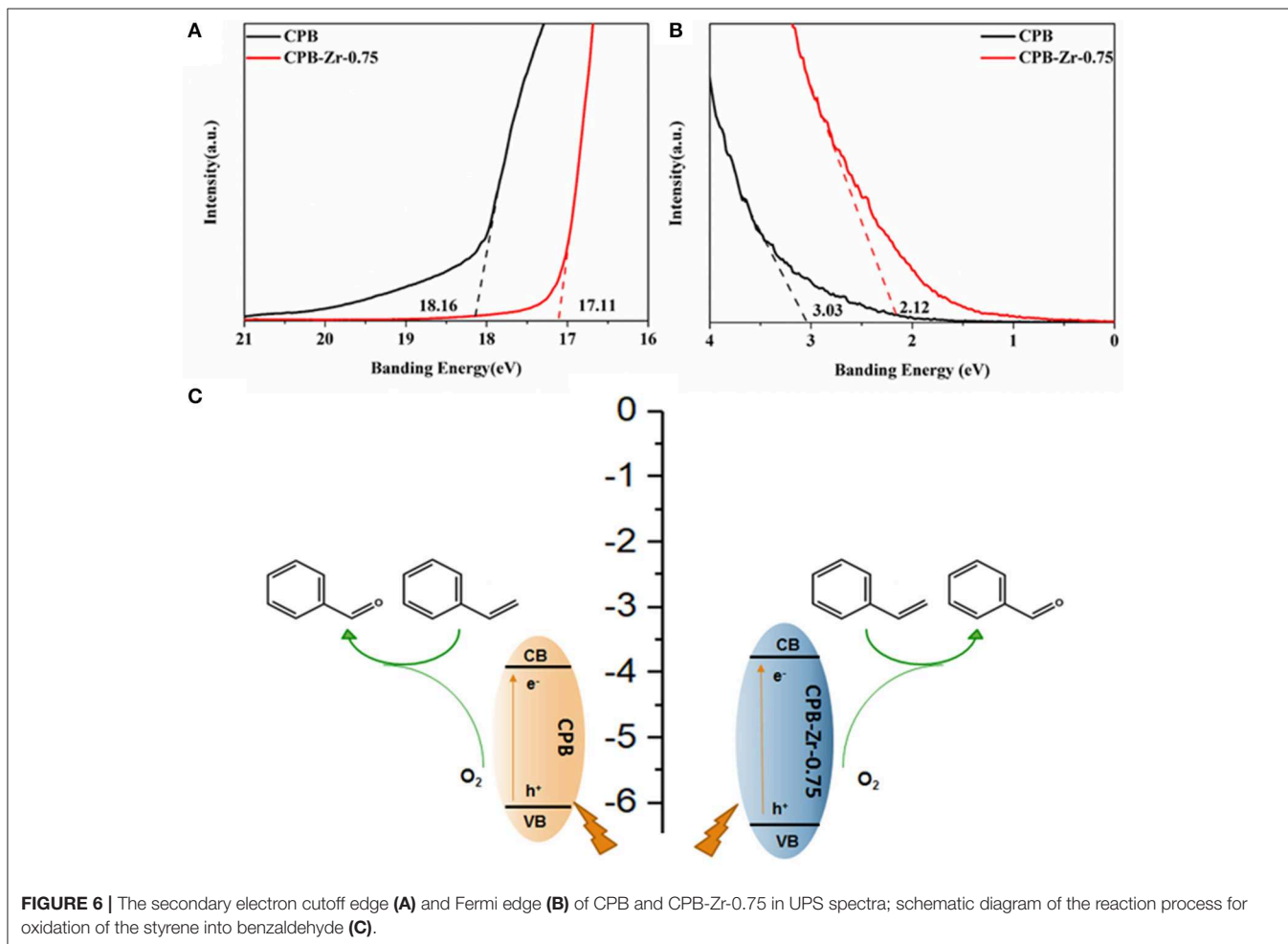

FIGURE 5 | Summarized catalytic activities of CPB and CPB-Zr-x (x = 0.25, 0.5, 0.75, 1).

reaction is almost identical to the fresh catalyst with only a slight blue shift, indicating the chemical rigidity of the PVSK after functionalization. MAPB and MAPB-Zr-x (x = 0.25, 0.5, 0.75, 1) are prepared by the same method as above, with photocatalytic experiments shown in **Figure S6**. The results suggest that that the chemical modification with ZrCl$_4$ can also improve the photocatalytic activity of MAPB toward the benzaldehyde production, although the baseline performance is not as good as that of CPB. The color of the MPB totally changes into white after the reaction, suggesting that the MAPB is not a robust photocatalyst as shown in **Figure S7**.

UPS Spectra Analysis and Reaction Process Investigation

To investigate the effect of ZrCl$_4$ on the catalytic performance of CPB, the UPS (**Figure 6**) determines the valence band positions of CPB and CPB-Zr-0.75. The energy level of the CPB and CPB-Zr-0.75 is determined by using ultraviolet photoelectron spectroscopy (UPS) with a photon energy of 21.20 eV. The work function can be determined from the difference between the photon energy and the binding energy of the secondary cutoff edge (**Figure 6A**). Therefore, the Fermi level (E$_f$) of CPB and CPB-Zr-0.75 can be determined to be −3.04 and −4.09 eV

FIGURE 6 | The secondary electron cutoff edge **(A)** and Fermi edge **(B)** of CPB and CPB-Zr-0.75 in UPS spectra; schematic diagram of the reaction process for oxidation of the styrene into benzaldehyde **(C)**.

relative to the vacuum level (E_{vac}), respectively. As shown in **Figure 6B**, the valence band (VB) spectra show that the valence band maxima (VBM) of CPB and CPB-Zr-0.75 are 3.03 and 2.12 eV below E_f, respectively. The bandgap of CPB and CPB-Zr-0.75 are calculated by UV-vis, approximately 2.27 eV and 2.56 eV, respectively. Therefore, the energy levels of the conduction bands of the two can be calculated as −3.8 and −3.65 eV, confirming that the Cl⁻ doped into CPB may result in the widening of bandgap.

Based on the experiment, the possible reaction process is then illustrated as the scheme in **Figure 6C**; the visible light activates the excitons inside the CPB. Upon the separation of electron–hole pairs, the electrons transport to the surface and react with adsorbed O_2 to generate activated oxygen species. Meanwhile, the styrene is adsorbed on the surface of the CPB and oxidized by the holes to the corresponding cationic radicals. The activated oxygen species then selectively oxidize the cationic radicals, finally leading to the formation of benzaldehyde. Due to the addition of $ZrCl_4$ precursor, the chemically modified CPB can promote the generation and transfer of excitons and carriers and hence accelerates the photocatalytic production rate of benzaldehyde.

CONCLUSION

In summary, we developed a surface functionalization strategy, by using $ZrCl_4$ as precursor to achieve the Zr-functionalization and the Cl doping at the same time to address the carrier transport and the light absorption issue for perovskite material. For the modified CPB nanosheet, the Cl doping that widens the bandgap and the surface modification that enhances the transport of photogenerated carriers can be accomplished by simply adding $ZrCl_4$ precursor in the synthesis, whereby the photocatalytic oxidation of styrene to benzaldehyde at room temperature can be largely improved. By promoting the energy transfer from CPB-Zr to O_2, the production rate can be improved from 376 up to 1,098 μmol g^{-1} h^{-1}, demonstrating the synergistic effect of Cl doping and surface modification in boosting the photocatalytic performance of CPB. In addition, this methodology can also work well for $MAPbBr_3$ and hence can be employed as a general approach to enhance the photocatalytic performance of PVSK-based catalysts.

DATA AVAILABILITY STATEMENT

The raw data supporting the conclusions of this article will be made available by the authors, without undue reservation, to any qualified researcher.

AUTHOR CONTRIBUTIONS

PQ and QW carried out most of the experiments and wrote the manuscript. YZ, YDa, YDo, and CC carried out part of the experiments. YL and QC designed the idea and wrote the manuscript.

SUPPLEMENTARY MATERIAL

The Supplementary Material for this article can be found online at: https://www.frontiersin.org/articles/10.3389/fchem. 2020.00130/full#supplementary-material

REFERENCES

Chen, Q., De Marco, N., Yang, Y., Song, T.-B., Chen, C.-C., Zhao, H., et al. (2015). Under the spotlight: the organic–inorganic hybrid halide perovskite for optoelectronic applications. *Nano Today* 10, 355–396. doi: 10.1016/j.nantod.2015.04.009

Dong, Q., Fang, Y., Shao, Y., Mulligan, P., Qiu, J., Cao, L., et al. (2015). Electron-hole diffusion lengths > 175 μm in SolutionGrown $CH_3NH_3PbI_3$ single crystals. *Science* 347, 967–970. doi: 10.1126/science.aaa5760

Feng, X., Ju, H., Song, T., Fang, T., Liu, W., and Huang, W. (2019). Highly efficient photocatalytic degradation performance of $CsPb(Br_{1-x}Cl_x)_3$-Au nanoheterostructures. *ACS Sustain. Chem. Eng.* 7, 5152–5156. doi: 10.1021/acssuschemeng.8b06023

Fu, Y., Xu, L., Shen, H., Yang, H., Zhang, F., Zhu, W., et al. (2016). Tunable catalytic properties of multi-metal-organic frameworks for aerobic styrene oxidation. *Chem. Eng. J.* 299, 135–141. doi: 10.1016/j.cej.2016.04.102

Gupta, R., Eswar, N. K., Modak, J. M., and Madras, G. (2017). Effect of morphology of zinc oxide in ZnO-CdS-Ag ternary nanocomposite towards photocatalytic

inactivation of *E. coli* under UV and visible light. *Chem. Eng. J.* 307, 966–980. doi: 10.1016/j.cej.2016.08.142

Hu, Z., Zhao, Y., Liu, J., Wang, J., Zhang, B., and Xiang, X. (2016). Ultrafine MnO_2 nanoparticles decorated on graphene oxide as a highly efficient and recyclable catalyst for aerobic oxidation of benzyl alcohol. *J. Colloid Interf. Sci.* 483, 26–33. doi: 10.1016/j.jcis.2016.08.010

Huang, H., Yuan, H., Janssen, K. P. F., Solís-Fernández, G., Wang, Y., Tan, C. Y. X., et al. (2018). Efficient and selective photocatalytic oxidation of benzylic alcohols with hybrid organic–inorganic perovskite materials. *ACS Energy Lett.* 3, 755–759. doi: 10.1021/acsenergylett.8b00131

Jin, L., and Oleg, V. P. (2015). Chlorine doping reduces electron–hole recombination in lead iodide perovskites: time-domain ab initio analysis. *J. Phys. Chem. Lett.* 6, 4463–4469. doi: 10.1021/acs.jpclett.5b02355

Luo, M., Yao, W., Huang, C., Wu, Q., and Xu, Q. (2015a). Shape-controlled synthesis of Pd nanoparticles for effective photocatalytic hydrogen production. *RSC Adv.* 5, 40892–40898. doi: 10.1039/C5RA06352C

Luo, M., Yao, W., Huang, C., Wu, Q., and Xu, Q. (2015b). Shape effects of Pt nanoparticles on hydrogen production via Pt/CdS photocatalysts under visible light. *J. Mater. Chem. A* 3, 13884–13891. doi: 10.1039/C5TA00218D

Lv, J., Shen, Y., Peng, L., Guo, X., and Ding, W. (2010). Exclusively selective oxidation of toluene to benzaldehyde on ceria nanocubes by molecular oxygen. *Chem. Commun.* 46, 5909–5911. doi: 10.1039/c0cc00777c

Majeed, I., Nadeem, M. A., Al-Oufi, M., Nadeem, M. A., Waterhouse, G. I. N., Badshah, A., et al. (2016). On the role of metal particle size and surface coverage for photo-catalytic hydrogen production: a case study of the Au/CdS system. *Appl. Catal. B Environ.* 182, 266–276. doi: 10.1016/j.apcatb.2015.09.039

Narayanan, S., Vijaya, J. J., Sivasanker, S., Ragupathi, C., Sankaranarayanan, T. M., and Kennedy, L. J. (2016). Hierarchical ZSM-5 catalytic performance evaluated in the selective oxidation of styrene to benzaldehyde using TBHP. *J. Porous Mater.* 23, 741–752. doi: 10.1007/s10934-016-0129-8

Nasrollahzadeh, M., Bagherzadeh, M., and Karimi, H. (2016). Preparation, characterization and catalytic activity of $CoFe_2O_4$ nanoparticles as a magnetically recoverable catalyst for selective oxidation of benzyl alcohol to benzaldehyde and reduction of organic dyes. *J. Col. Inter. Sci.* 465, 271–278. doi: 10.1016/j.jcis.2015.11.074

Oliveira, A. P. S., Gomes, I. S., Neto, A. S. B., Oliveira, A. C., Filho, J. M., Saraiva, G. D., et al. (2017). Catalytic performance of MnFeSi composite in selective oxidation of styrene, ethylbenzene and benzyl alcohol. *Mol. Catal.* 436, 29–42. doi: 10.1016/j.mcat.2017.04.007

Shamsi, J., Dang, Z., Bianchini, P., Canale, C., Di Stasio, F., Brescia, R., et al. (2016). Colloidal synthesis of quantum confined single crystal $CsPbBr_3$ nanosheets with lateral size control up to the micrometer range. *J. Am. Chem. Soc.* 138, 7240–7243. doi: 10.1021/jacs.6b03166

Singh, B., and Sinha, A. K. (2014). Synthesis of hierarchical mesoporous vanadium silicate-1 zeolite catalysts for styrene epoxidation with organic hydroperoxide. *J. Mater. Chem. A* 2, 1930–1939. doi: 10.1039/C3TA13451B

Tong, J., Li, W., Bo, L., Wang, H., Hu, Y., Zhang, Z., et al. (2016). Selective oxidation of styrene catalyzed by cerium-doped cobalt ferrite nanocrystals with greatly enhanced catalytic performance. *J. Catal.* 344, 474–481. doi: 10.1016/j.jcat.2016.10.003

Wang, P., Sheng, Y., Wang, F., and Yu, H. (2018). Synergistic effect of electron-transfer mediator and interfacial catalytic active-site for the enhanced H_2-evolution performance: a case study of CdS-Au photocatalyst. *Appl. Catal. B Environ.* 220, 561–569. doi: 10.1016/j.apcatb.2017.08.080

Wang, Q., Tao, L., Jiang, X., Wang, M., and Shen, Y. (2019). Graphene oxide wrapped $CH_3NH_3PbBr_3$ perovskite quantum dots hybrid for photoelectrochemical CO_2 reduction in organic solvents. *Appl. Surf. Sci.* 465, 607–613. doi: 10.1016/j.apsusc.2018.09.215

Wang, X., Huang, Y., Liao, J., Jiang, Y., Zhou, L., Zhang, X., et al. (2019). *In situ* construction of a Cs_2SnI_6 perovskite nanocrystal/SnS_2 nanosheet heterojunction with boosted interfacial charge transfer. *J. Am. Chem. Soc.* 141, 13434–13441. doi: 10.1021/jacs.9b04482

Xing, G., Mathews, N., Sun, S., Lim, S. S., Lam, Y. M., Gratzel, M., et al. (2013). Long-range balanced electron- and hole-transport lengths in organic-inorganic $CH_3NH_3PbI_3$. *Science* 342, 344–347. doi: 10.1126/science.1243167

Xu, S., Jiang, R., Jiang, S., and Gao, Y. (2016). Communication—anion-conductive perfluoroheteroaromatic composite membranes: high chemical stability under strong alkaline conditions. *J. Electrochem. Soc.* 163, F688–F690. doi: 10.1149/2.1261607jes

Yadav, G. D., and Haldavanekar, B. V. (1997). Mechanistic and kinetic investigation of liquid-liquid phase transfer catalyzed oxidation of benzyl chloride to benzaldehyde. *J. Phys. Chem. A* 101, 36–48. doi: 10.1021/jp961678x

Yang, Y., Ostrowski, D. P., France, R. M., Zhu, K., van de Lagemaat, J., Luther, J. M., et al. (2016). Observation of a Hot-Phonon Bottleneck in lead-iodide perovskites. *Nat. Photonics* 10, 53–59. doi: 10.1038/nphoton.2015.213

Yang, Y., Yang, M., Li, Z., Crisp, R., Zhu, K., and Beard, M. C. (2015). Comparison of recombination dynamics in $CH_3NH_3PbBr_3$ and $CH_3NH_3PbI_3$ perovskites films: influence of exciton binding energy. *J. Phys. Chem. Lett.* 6, 4688–4692. doi: 10.1021/acs.jpclett.5b02290

Yang, Y., Yang, M., Moore, D. T., Yan, Y., Miller, E. M., Zhu, K., et al. (2017). Top and bottom surfaces limit carrier lifetime in lead iodide provskite films. *Nat. Energy* 2:16207. doi: 10.1038/nenergy.2016.207

Zhang, F., Zhong, H., Chen, C., Wu, X.-G., Hu, X., Huang, H., et al. (2015). Brightly luminescent and color–tunable colloidal $CH_3NH_3PbX_3$ (X = Br, I, Cl) quantum dots: potential alternatives for display technology. *ACS Nano* 9, 4533–4542. doi: 10.1021/acsnano.5b01154

Zhao, J., Nail, B. A., Holmes, M. A., and Osterloh, F. E. (2016). Use of surface photovoltage spectroscopy to measure built-in voltage, space charge layer width, and effective band gap in cdse quantum dot films. *J. Phys. Chem. Lett.* 7, 3335–3340. doi: 10.1021/acs.jpclett.6b01569

Zhu, X., Lin,Y., Sun, Y., Beard, M. C., and Yan, Y. (2019). Lead-halide perovskites for photocatalytic α-alkylation of aldehydes. *J. Am. Chem. Soc.* 141, 733–738. doi: 10.1021/jacs.8b08720